Central Tracking System for Asian Joint Linear Collider

Norik Khalatyan
High Energy Accelerator Research Organization (KEK),
Tsukuba, 305-0801, Japan

Abstract

Past and current status of JLC-CDC activity is presented, which includes measurements of gravitational and electrostatic sags for a 4.6m test chamber, its cosmic ray tests, designing of stereo-wire geometry, and preliminary results of Lorentz angle and two-track separation measurements.

1 Introduction

One of the most important goals of experiments at our Asian Joint Linear Collider[1] is to discover and study the Higgs boson. In particular, if one wants to confirm the narrowness of the Higgs boson by measuring the distribution of the recoil mass opposite to the lepton pair from the Z^0 boson decay in the process $e^+e^- \to H^0Z^0$, the recoil mass resolution should at least be as good as the beam energy spread of the collider.

This requires a high resolution central tracker with a momentum resolution of $\sigma_{p_T}/p_T \sim 10^{-4} \times p_T(\text{GeV})$. Such a tracking chamber becomes as large as 2.3 m in radius, even if we assume 100 sampling points with a spatial resolution of 100μm per wire in a magnetic field of as high as 2 T. In addition, to ensure this momentum resolution over a polar angle range of $45° < \theta < 135°$, the chamber has to be as long as 4.6 m.

In order to fulfill the physics requirements, we need to achieve the following performance goals: $\sigma_{r\phi} \simeq 100$ μm, $\sigma_{rz} \simeq 1$ mm, and two track separation better than 2 mm. The second and the third of the above goals are to ensure good track-cluster matching in a jetty environment. One possible approach to realizing these design goals is to use a slow gas mixture with a small Lorentz angle and a mini-jet cell structure to allow stereo wires for z-coordinate measurements. A large cylindrical drift chamber with small jet cells is a candidate central tracking device to fulfill these requirements.

The paper is organized as follows. Measurements of gravitational and electrostatic sags for a 4.6m test chamber are described in Section 2 [1]. A method to calculate the wire sags knowing the initial position of and tension and high voltage on each wire is developed. Section 3 is devoted to the performance of a 4.6 m-long drift chamber filled with a CO_2 iso-butane (90 : 10) mixture studied using cosmic ray data [2]. In Section 4 common problems in designing stereo-wire geometry for a long cylindrical drift chamber with small jet cells are described and possible ways to approach them are discussed in detail [3]. Among these problems, special emphasis is put on the surface field variation

[1]Hereafter we call this Joint Linear Collider as JLC in short.

along an anode wire due to the geometrical deformation of the cell structure. These field variations are translated into gas gain variation along the stereo wires and used to constrain the stereo geometry. Section 5 is devoted to Lorentz angle measurement of the CO_2/Isobutane gas mixture [4]. Also we propose a new Lorentz angle measurement system by using two simultaneous laser beams. Preliminary results of two track separation experiment by using a small test chamber (*Baby*) are presented in Section 5 [5]. Finally Section 6 summarizes our results and concludes this paper.

2 Gravitational and Electrostatic Wire Sags for a 4.6 Meter-Long Drift Chamber

Due to substantial gravitational and electrostatic sags, achieving a spatial resolution of 100 μm/wire for a 4.6 m long chamber is quite non-trivial. We need to be able to predict wire positions very precisely under the influence of gravitational and electrostatic forces.

We have been developing a software program to predict wire displacement, knowing the cell structure, wire tension, and high voltage on each wire. The validity of the prediction has to be proved experimentally. We have developed a wire tension and position measurement system and measured wire tensions, gravitational and electrostatic sags for a 4.6 m long test chamber (see Fig. 1). The results of the measurements were then compared with the predictions.

Figure 1: 4.6 m CDC test chamber with wire position measurement system.

2.1 Test Chamber Parameters

We designed a mini-jet cell so as to realize the design goals ignoring possible wire sag effects, since the electric field can be calculated to a good approximation in this way, if all the wires have the same gravitational sags.

A possible cell design is shown in Fig. 2-(a) which also specifies our wire naming convention to be used hereafter. The cell has 5 sense wires ($S1$ to $S5$) held at 2.5 kV and

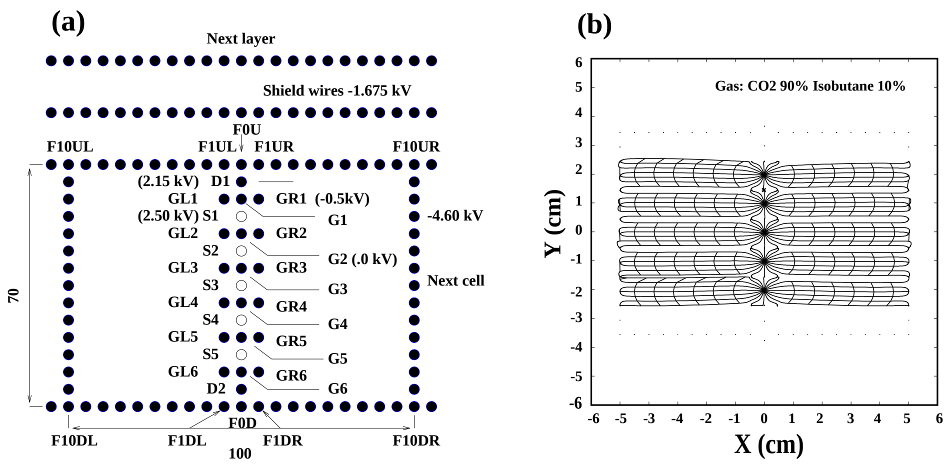

Figure 2: (a) possible mini-jet cell structure and (b) corresponding drift lines.

spaced 1 cm, with each surrounded by ground wires ($G1$ to $G6$) in the sense wire plane and grid wires ($GL1$ to $GL6$ and $GR1$ to $GR6$) at -0.5 kV placed 5 mm away from it. The two dummy sense wires ($D1$ and $D2$) at the both ends of the sense wire plane are held at 2.15 kV and stabilize the upper- and the lower-most sense wires ($S1$ and $S5$). The maximum drift length is 5 cm where the drift field is produced by 10 field shaping wires ($F1**$ to $F10**$) whose potentials change linearly in this order from -0.5 kV to -4.6 kV, and by left and right edge field wires held at -4.6 kV. The wire diameter is 30 μm for sense wires and 125 μm for the others. The high voltages on the wires were chosen so as to get as uniform a drift field as possible with minimum electrostatic forces, while keeping a reasonable gas gain for a chamber gas mixture of 90%CO_2 and 10% Isobutane. Fig. 2-(b) plots the drift lines calculated with a drift chamber simulation program GARFIELD. Our 4.6 m long test chamber has seven identical cells with the cell parameters described above.

2.2 Gravitational and Electrostatic Sag Measurements

As seen in Fig. 1, we used two CCD cameras, one for horizontal and the other for vertical position measurements. Each of these two cameras has an area of sight of 1 mm $\times$ 1 mm and a focal depth of $\simeq$ 1 mm, which is about 1 m away from the front face of the camera.

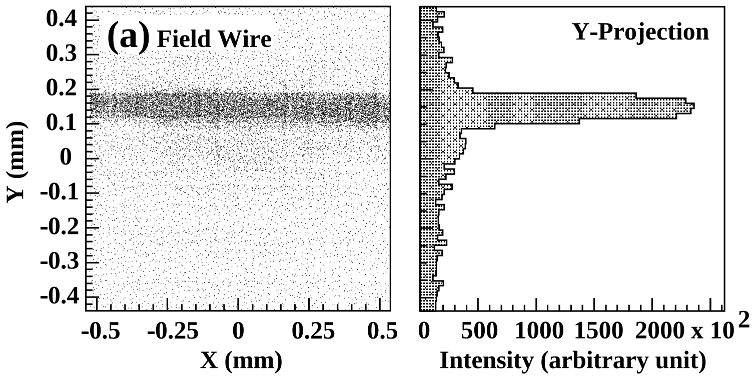

Figure 3: Typical CCD images for a 125 μm field wire.

Typical field and sense wire images from the CCD cameras are shown in Figs.3-(a) and -(b), demonstrating the resolution of our system.

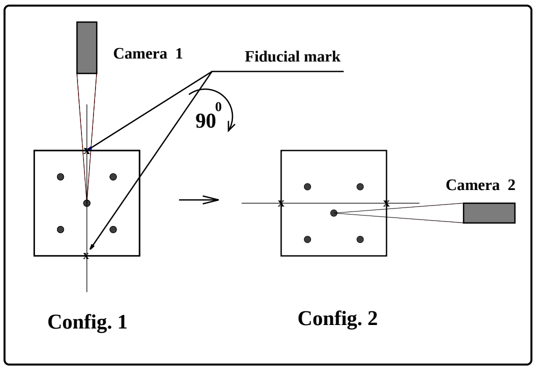

Figure 4: Principle of gravitational sag measurements

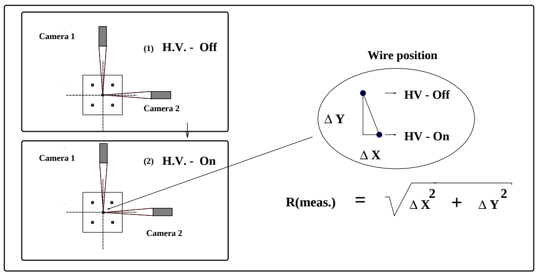

Figure 5: Schematic view of the electrostatic sag measurements.

Fig. 4 illustrates our measurement scheme of the *gravitational* sag of a wire. The measurement goes as follows. Using the vertical camera, we first put fiducial marks on the chamber windows in such a way that the line connecting them passes through the wire in question (configuration 1 in Fig. 4). Then we rotate the test chamber by 90° and determine the wire deflection due to gravitational sag by measuring the wire position relative to the line connecting the fiducial marks, using the horizontal camera (config.2 in Fig. 4).

We measured the gravitational sags for 1.5 years after the wire stringing. The average gravitational sags for field and sense wires were 600μm and 353μm, respectively.

Our measurement scheme of *electrostatic* sag is sketched in Fig. 5. We first get a wire in sight on both the horizontal and vertical cameras with high voltages off. Then we measure the horizontal (ΔX) and vertical (ΔY) displacements in the camera screens after turning on the high voltages.

2.3 Results

In Fig.6 we compare the measurements and predictions for a few field wires which are on the left and right sides of the sense wire plane. There is a good agreement not only in the magnitude of deflection but also in its direction for each one of these field wires.

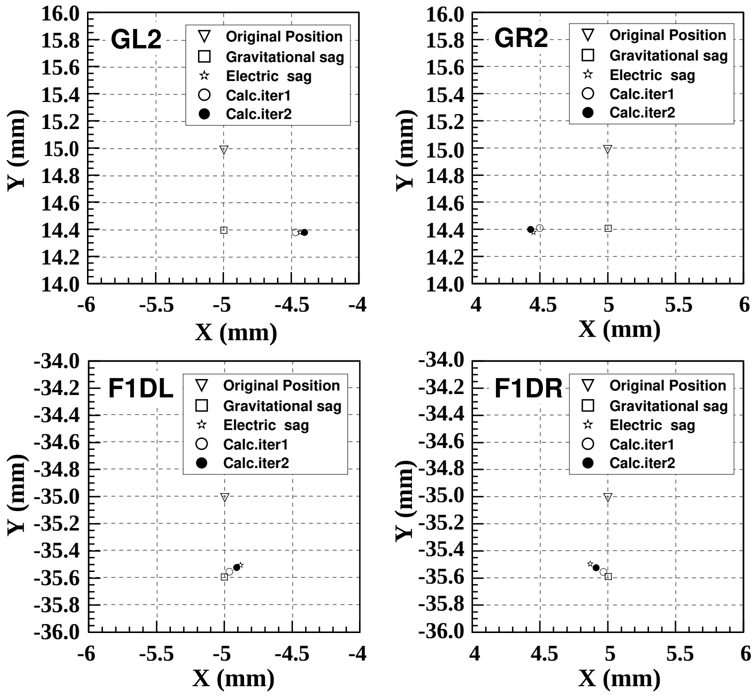

Figure 6: Measured positions of some representative field wires at the endplates ($\bigtriangledown$), with gravitational sags (o) before and ($\star$) after electrostatic sags, compared with calculations: iterations 1($\circ$) and 2 ($\bullet$).

3 Cosmic Ray Test

The next question is whether we can actually achieve the required spatial resolution over the full length of the 4.6 m-long chamber, armed with the quantitative knowledge on the wire sags. In order to confirm this, we studied the performance of the test chamber using cosmic rays.

3.1 Experimental Results

The pulse shapes for a typical cosmic-ray track is shown in Fig.7. This flash-ADC fully covers the maximum drift time of the test chamber (about 6 μsec) and provides a high enough sampling frequency to ensure a good enough resolution (2 nsec corresponding to 16 μm drift equivalent).

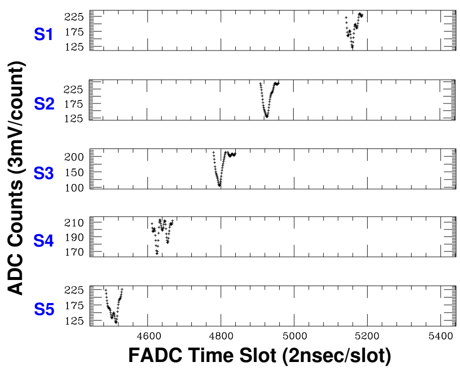

Figure 7: Pulse shapes for a typical cosmic-ray track.

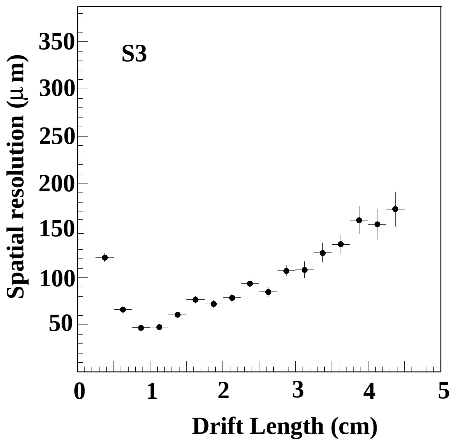

Figure 8: Spatial resolution of the central sense wire ($S3$) as a function of the drift distance.

3.2 Spatial Resolution

The overall intrinsic spatial resolutions for individual sense wires are summarized in Table 1. Inspection of the table tells us that the overall resolutions are around 100μm, satisfying our performance goal at least locally. A similar analysis was carried out for tracks passing though the central cell near the both ends of the wires, in order to make sure that the performance goal be satisfied over the full length of the chamber.

Table 1: Summary of spatial resolutions

Wire Number	Center	Ends	Inclined
S1	$117 \pm 23(\mu m)$	$163 \pm 75(\mu m)$	$94 \pm 38(\mu m)$
S2	$103 \pm 7(\mu m)$	$136 \pm 52(\mu m)$	$95 \pm 15(\mu m)$
S3	$103 \pm 9(\mu m)$	$120 \pm 22(\mu m)$	$102 \pm 19(\mu m)$
S4	$98 \pm 9(\mu m)$	$119 \pm 22(\mu m)$	$90 \pm 19(\mu m)$
S5	$109 \pm 16(\mu m)$	$132 \pm 45(\mu m)$	$105 \pm 39(\mu m)$

The intrinsic resolutions may also depend upon the incident angle of a track to the sense wires. In order to investigate this effect, we set the two trigger counters in the middle of the chamber but slightly displaced so as to primarily sample inclined tracks having an incident angle of around 45° to the wires. This incident angle (45°) corresponds to the maximum dip angle with the full number of sense wires for our current design of the JLC central tracker. The spatial resolution of the central sense wire ($S3$) as a function of drift length is shown in Fig. 8.

The overall intrinsic spatial resolutions are summarized in Table 1. We thus confirmed that a spatial resolution of about 100μm up to an incident angle of 45°.

4 Stereo-Wire Geometry for a Long Cylindrical Drift Chamber with Small Jet Cells

From the track-cluster matching point of view, what we are concerned most is track extrapolation errors, which depend on both r-ϕ and z resolutions. Improvement of the latter necessitates introduction of stereo wires, since the z resolution in charge division or time difference readout is typically 1 % of the wire length or worse, which is a few cm in the linear collider use.

The spatial resolution per wire in the axial direction σ_z is given by

$$\sigma_z = \sigma_{r\phi} / \tan\alpha \tag{1}$$

in the case of stereo wires with a stereo angle α, where $\sigma_{r\phi}$ is spatial resolution in the r-ϕ plane per wire. Apparently the larger the stereo angle becomes the better the spatial resolution per wire in the axial direction. There are, however, various restrictions to the stereo angle which are the main topics of this Section.

4.0.1 Global Stereo-Geometrical Parameters

At this point we have a rough idea about basic parameters describing the JLC-CDC: the inner and outer radii, the length, the number of sampling points, and the $r\phi$ spatial resolution per wire. In order to decide the stereo geometry, we further need to know the super-layer layout of the chamber and problems introduced by the use of finite stereo angles. A stereo layer can be formed by rotating the end point of each wire belonging to this layer by a small angle ($\Delta\phi$) with the other end point fixed, as illustrated in Fig.9.

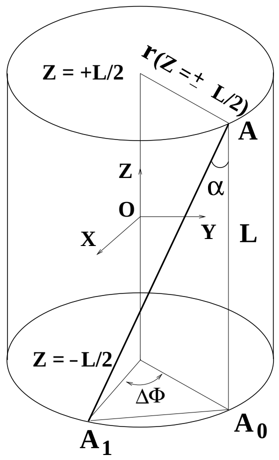

Figure 9: 3-dimensional view of a single stereo wire.

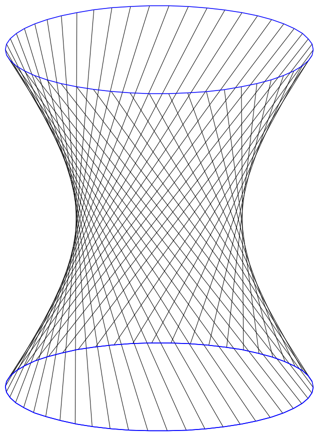

Figure 10: Formation of a hyperboloidal surface due to stereo wires.

The otherwise cylindrical surface of this wire layer turns into a hyperboloidal surface as shown in Fig.10. As a result, both the azimuthal angle and the radial position of the stereo wire becomes z-dependent. This inhomogeneity distorts the electric field to some extent and limits the maximum possible stereo angle, thereby restricting the z resolution σ_z. Fig.11 demonstrates how a single stereo cell structure deforms as one moves from one endplate to the other, where $ABCD$ and $A_1B_1C_1D_1$ are the cross sections of a single stereo cell at the end plates ($z = \pm L/2$). $A_2B_2C_2D_2$ is that of the same stereo cell inbetween ($-L/2 < Z < +L/2$). This z-dependent geometrical deformation of the stereo cell is parametrized by a so called shrink factor and imposes another important restriction on the possible range of stereo angles.

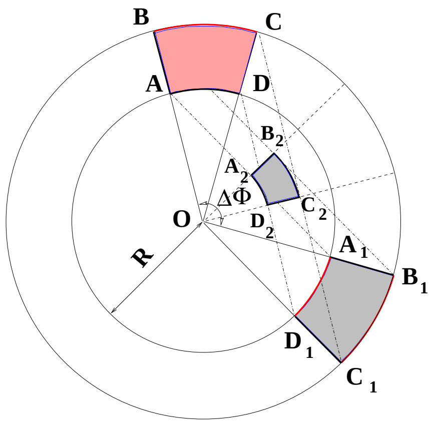

Figure 11: Exaggerated illustration of the stereo-cell formation through rotation by an angle $\Delta\phi$ and its deformation along the wires.

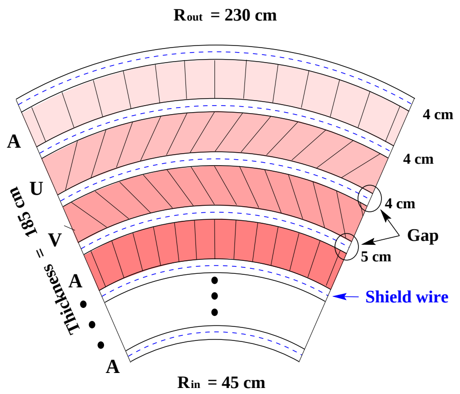

Figure 12: A possible super-layer layout for the central tracking system of the JLC.

4.1 Illustration of Stereo Geometry Determination

4.1.1 A Possible Central Tracker for JLC

Basic parameters of a possible JLC central tracker read $B = 2\ T$, $r_{in} = 45$ cm, $r_{out} = 230$ cm, $L = 460$ cm, $n = 80$, and $\sigma_{r\phi} = 100\ \mu$m, whose feasibility is the key issue of our on-going R&D. The tracker consists of 6 axial and 10 stereo super-layers, each having 5 anode wires, arranged with increasing r in the following order: $AVUAVUAVUAVUAVUA$, where A, V, and U again denote an axial super-layer, stereo super-layers with stereo angles of $+\alpha$ and $-\alpha$, respectively. The gap between adjacent super-layers is correlated with the stereo angle and is equal to either 4.0 or 5.0 cm at the endplates, depending on its radial location: the U-to-A and the V-to-U gaps are equal to 4.0 cm, while the A-to-V is set at 5.0 cm (see Fig.12).

4.1.2 Geometrical Limitation to the Stereo Angle

It is already clear that there is a definite geometrical limit to the maximum possible stereo angle: the stereo angle should be small enough to avoid mechanical contact of wires belonging to different layers. The decisive parameter is therefore the minimum distance between shielding wires and the stereo wires. This is more important for the A-to-V gaps, since an A super-layer stays as a cylinder, while the V super-layer surrounding it shrinks in the middle: it changes its shape to a hyperboloid. In the above mentioned JLC example, the shielding wires are 2.5 cm away from the nearest stereo super-layer (V) at the both wire ends. Along the length of the chamber the distance between the innermost stereo layer belonging to a V super-layer and the adjacent layer of the shielding wires decreases as a quadratic function of z and attains its minimum at $z = 0$.

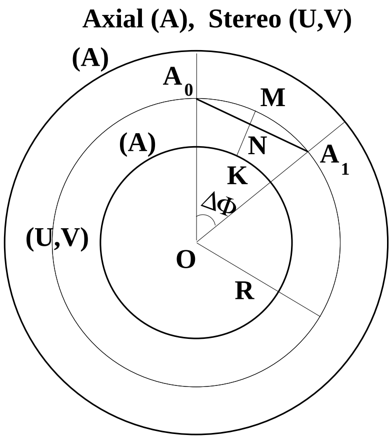

Figure 13: r-ϕ projection of a stereo wire (A_0A_1): MN is the maximum displacement of the stereo wire.

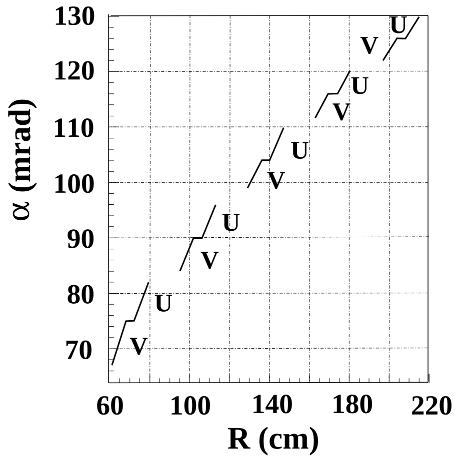

Figure 14: Upper limit of the stereo angle as a function of the radius for all of the 10 stereo super-layers.

Fig.13 illustrates the $r\phi$ projection (A_0A_1) of a single stereo wire. Then we have

$$A_0A_1 = L \cdot \tan\alpha, \tag{2}$$

where the chamber length is $L = 4.6$ m in the JLC example (see Fig.9). MN is the maximum displacement of the stereo wire with respect to its original position on the endplates and corresponds to the middle point ($z = 0$) along the wire:

$$MN \equiv d \quad = \quad R - \sqrt{R^2 - \frac{L^2 \cdot \tan^2\alpha}{4}}, \tag{3}$$

where the nominal radius $R = r(z = \pm L/2)$ is the radial position of the stereo wire at the endplates (see Fig.9).

In order to prevent the stereo wire from touching any shielding wire, this maximum displacement MN should be less than the nominal distance between the shielding and stereo wires measured at the endplates. The maximum displacement MN, however, strongly depends on the stereo angle α and the nominal radius R.

Fig.14 shows the upper limit of the stereo angle as a function of the radial position of each super-layer. From these we can read off the geometrical upper limit on the stereo angle for each stereo super-layer. As pointed out above, it should be noted here again that the stereo angle varies even within a single cell and it grows linearly with the radial position. On the other hand, $\Delta\phi$ is constant within a single super-layer.

4.1.3 Z-dependent Geometrical Deformation of Stereo Cells

As shown earlier, the wires belonging to a stereo layer form a hyperboloidal surface. Consequently, any stereo cell shrinks as one moves from an endplate to the middle of the wires by the following formula:

$$f(z) = \frac{\sqrt{R^2 + \tan^2\alpha\,(z^2 - (L/2)^2))}}{R}. \tag{4}$$

In this formula the shrink factor f is a function of z, R, and α.

The z-dependent geometrical deformation of the stereo cell induces variation of the surface field on the sense wires in it, thereby introducing gain nonuniformity along the wires. We calculated the surface field variation on the sense wires, using the drift chamber simulation program, GARFIELD. Fig.15 plots the calculated surface fields against the z coordinate. The maximum variation of the surface field is $\Delta E/E \simeq 0.43$ %.

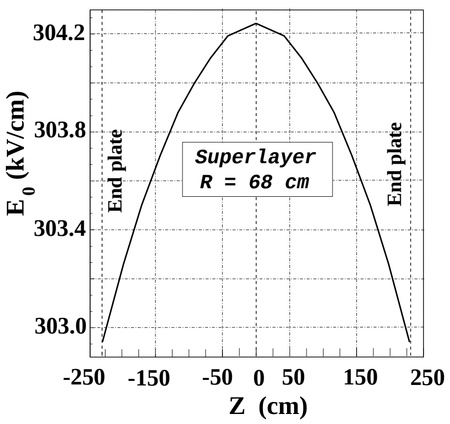

Figure 15: Surface field as a function of z for a sense wire in the innermost stereo super-layer at $r = 68$ cm.

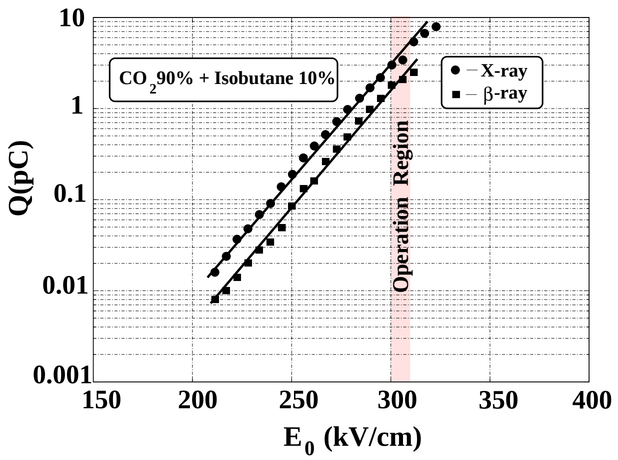

Figure 16: Signal charge as a function of the surface field on a sense wire.

4.2 Gas Gain Variation along Stereo Wires

Now that we know the surface field variation along any wire, we can study its z-dependent gas gain variation and discuss the operation feasibility of the chamber, provided that the relation of the surface field to the gas gain is known. Conversely, the stereo angle should be so determined to make the gain variation acceptable.

We have measured the gas gain for the CO_2(90%)-Isobutane (10%) mixture, by using a single wire proportional counter. This gas mixture is a possible candidate for the JLC central tracker because of its very small diffusion coefficients. The counter is made of an aluminum cathode tube with a 10 mm inner diameter and a gold-plated tungsten anode wire with a 30 μm diameter. For the ^{55}Fe X-rays (5.9 keV) and ^{90}Sr β-rays, the charges collected on the anode within 1 μsec were measured as a function of the applied voltage.

The results of the measurements are depicted in Fig.16, where the collected charge Q is plotted as a function of the anode surface field E_0.

These data are fitted to the following empirical formula:

$$\ln Q = a + bE_0, \tag{5}$$

where a and b are the parameters to be determined. From these data, we obtain the following relation:

$$\frac{\Delta Q}{Q} = (15 \sim 20)\left(\frac{dE_0}{E_0}\right) \tag{6}$$

around $E_0 \simeq 300$ kV/cm, where the gas gain is about 10^4.

By combining these results with the surface field variations calculated in the previous subsubsections, we estimate the gain variation of the stereo wire due to the stereo geometry to be at most 8 % which is acceptable.

5 Lorentz Angle Measurements

5.1 Lorentz Angle and Single Cell Design

When a charged particle passes through a cell of the JLC-CDC, the charged particle ionizes molecules of chamber gas along its track. After that, this primary electrons drift toward sense wires. By measuring drift times of these electrons, we know where the charged particle has passed.

In order to decide its momentum from the curvature of the track, the CDC should be placed in a magnetic field. However, this magnetic field also bends drift lines of electrons. Fig.17 shows drift lines in our cell which were calculated with the GARFIELD program. The left picture gives drift lines without magnetic field. Those drift lines are parallel to the electric field. The right picture shows the drift lines at a magnetic field of 2 T. Those drift lines have a finite deflection angle to the electric field, and we call this angle the Lorentz angle. The Lorentz angle depends on electric and magnetic fields, as well as gas mixture.

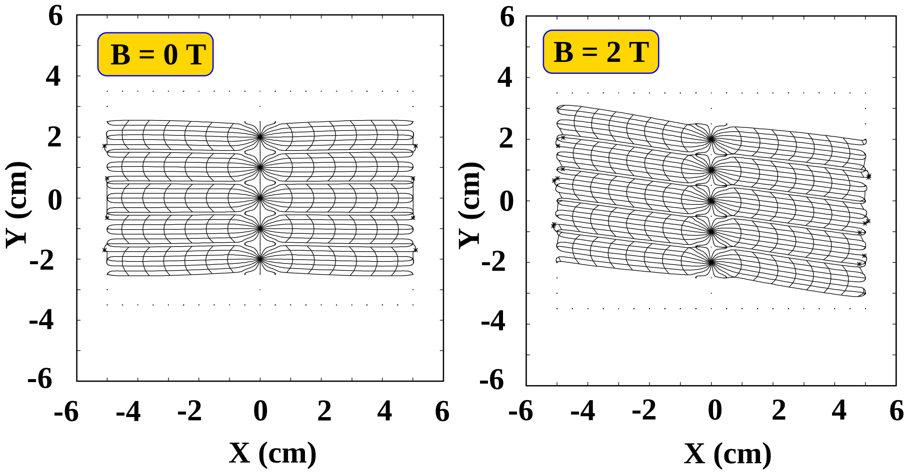

Figure 17: GARFIELD results of Drift lines (CO_2-Isobutane(90:10))

Fig.17 also shows acceptance of the Lorentz angle. When the Lorentz angle becomes exceedingly bigger, some drift electrons are absorbed by field wires before reaching a sense wire. Although we have a solution for this problem, to incline cells along with drift lines, we prefer to use a gas mixture which has small enough Lorentz angle to keep the original cell shape. It contributes to keep good two-track separation.

The purpose of the Lorentz angle measurement is to get the actual value of Lorentz angle for our gas mixture and to confirm the reliability of the GARFIELD simulation.

5.2 Experimental Procedure

The principle of the Lorentz angle measurement is illustrated in Fig.18. The anode wire is placed along the x-axis, orthogonal to the magnetic-field. The laser beam incidents between copper plates, and causes ionization at the center of the copper plate windows. Owing to the homogeneous electric-field by copper plates, primary electrons drift toward anode wire, and its path is deflected along the x-axis by the magnetic-field. When those primary electrons approach the anode wire, gas multiplication process begins and an avalanche covers the small location of anode wire, which then induces charges on the cathode pads simultaneously.

In order to eliminate the influence of the electric-field inhomogenity near the anode wire, the Lorentz angle is calculated using the following formula:

$$tan\alpha = \frac{G_{z_2} - G_{z_1}}{z_2 - z_1} \tag{7}$$

where z_1 and z_2 are the laser beam positions, G_{z_1} and G_{z_2} are the arrival points of drift electrons along the x-axis.

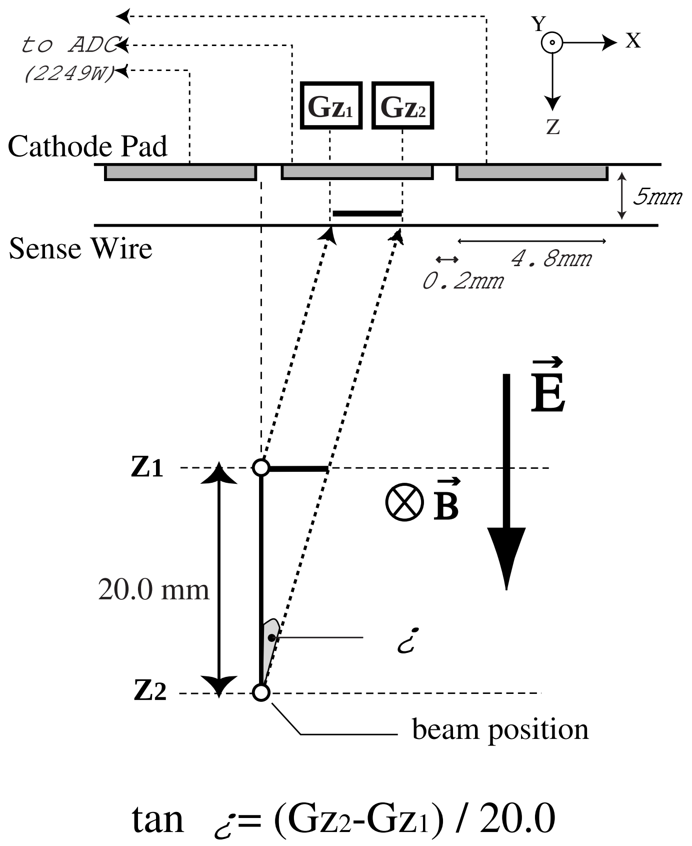

Figure 18: Illustration of Lorentz angle measurement

5.3 Experimental Results

We measured the Lorentz angle for CO_2-Isobutane mixtures, 90:10, 95:5, and 85:15, in the electric-field range between 0.2 and 2.0 kV/cm and under the magnetic-fields between 0 and 1.5 T. All measurements have been done at the room temperature and at the atmospheric pressures. Fig.19 shows the results of Lorentz angle measurements for different magnetic fields as a function of electric field together with the GARFIELD simulation. Due to the limitation of USHIWAKA-magnet, the highest magnet field was 1.5 T.

The extrapolation to 2.0 T was done by a linear fitting. Fig.20 shows the extrapolated value at 2 T, where the gas mixture is CO_2-isobutane (90:10) and the electric-field is 1.0 kV/cm.

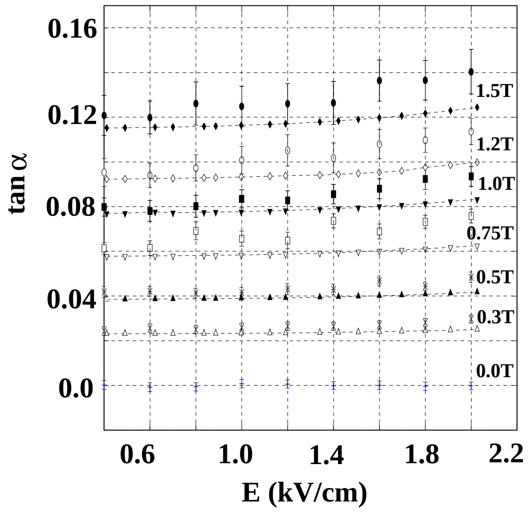

Figure 19: Comparison with GARFIELD simulations for the CO_2-isobutane (90:10).

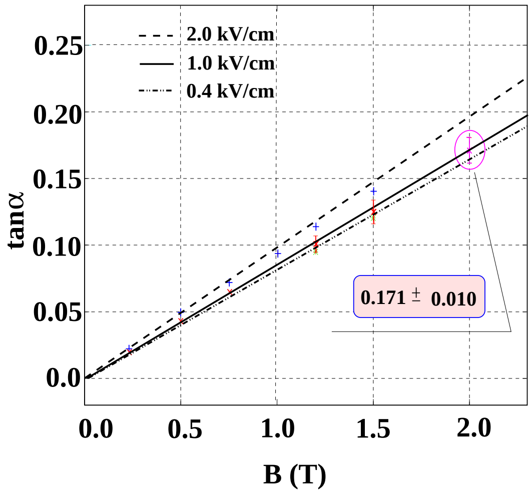

Figure 20: Lorentz angle extrapolated to 2.0T for the CO_2-isobutane (90:10).

5.4 Discussion

Fig.19 implies a potential problem: the errors on tanα grows as the magnetic field increases. Fig.21 shows a comparison of the time dependence of G and ADC values at 0.3 T and 1.5 T, which shows evident difference on its behavior. For all data at the high magnetic-field, G makes vibration whose amplitude depends on the magnetic field and its frequency is very unstable. The frequency has no correlation with the magnetic-field and the electric-field, has no reproducibility, and is much slower than 10 Hz(= data taking rate).

Another possibility is instability of the beam position. If the incident beam position fluctuates, both deflected-value of the x and drift distance may change event by event. During measurements, we observed the USHIWAKA magnet was vibrating at the high magnetic field.

In order to study this problem and improve our measurement, we propose a new experiment in the next subsection.

5.5 Proposals of the Next Experiment

We assumed that the vibration of center of gravity G comes from the instability of the beam position. If a pair of center of gravity data for different drift lengths can be obtained simultaneously, the values $(z_2 - z_1)$ and $(G_{z_2} - G_{z_1})$ will be stable. For example, when z_1 moves along x-axis, z_2 will moves in the same direction and the same amount simultaneously, so that the fluctuation in z_1 and z_2 should cancel each other. Therefore, we propose a two-laser-beam system.

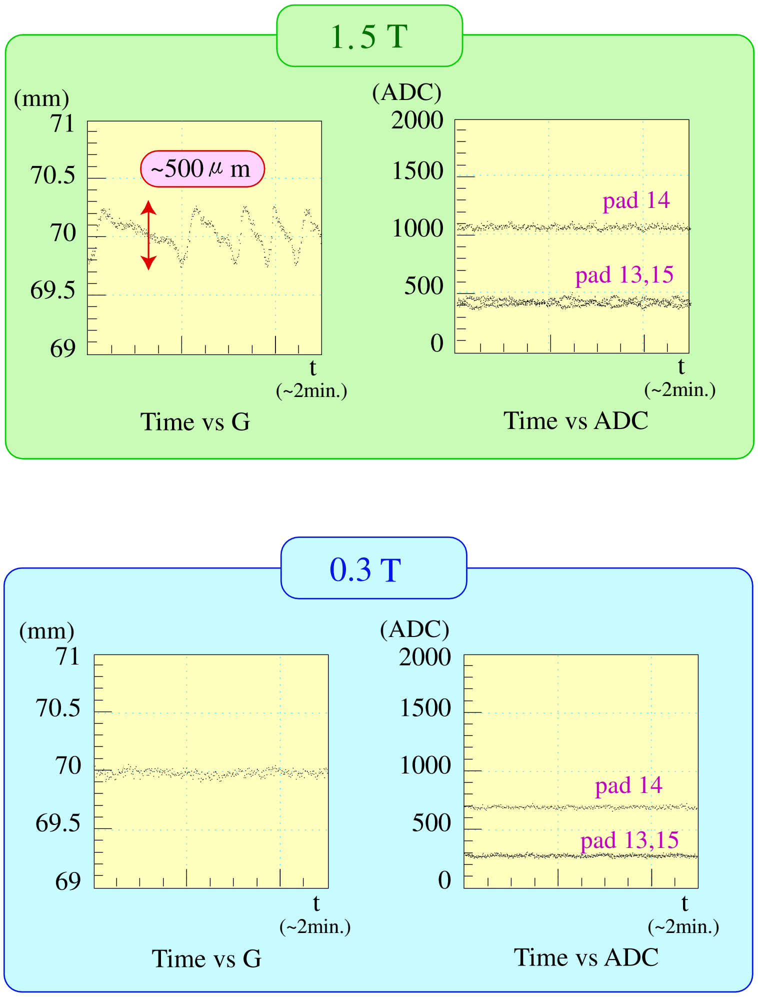

Figure 21: Comparison of time dependence of center of gravity at 0.3 T and 1.5 T

Fig.22 shows the principle of our new Lorentz angle measurement system. It is almost same as the present measurement system except that both G_{z_1} and G_{z_2} can be obtained by one shot of laser beam. On the other hand, this improvement requires a new data acquisition system which can record two separate signals simultaneously as a single event. In order to fulfill this requirement, we propose to use Flash ADCs. The induced charges on the cathode pads can then be obtained by integrating such pulse shapes. Then, the center of gravity can be calculated as before.

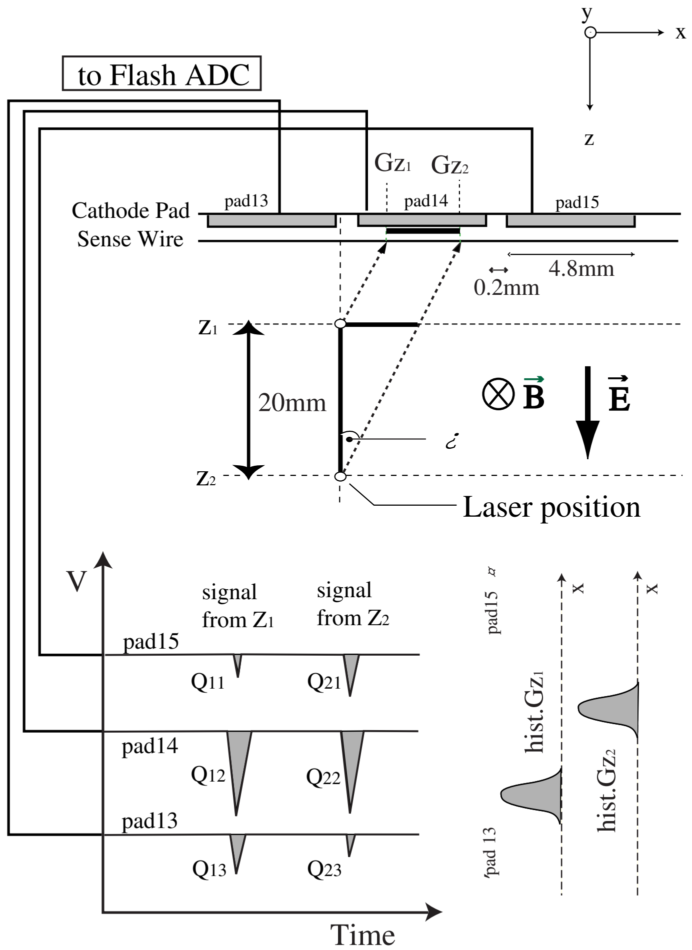

Figure 22: Illustration of the new Lorentz angle measurement system.

6 Two-Track Separation Experiment

The study presented in this section focuses on the basic chamber performance including spatial resulution, efficiency, and two-track separation as determined by the cell design, gas mixture choice, etc. We have built a test chamber with a candidate cell structure filled with a possible gas mixture CO_2/Isobutane(90:10) for this purpose and made a beam test with special emphasis put on two-track separation study. The beam test was carried out at the $\gamma 2$ beam line of the 1.3-GeV KEK-Tanashi Electron Synchrotron (ES), using an extracted electron beam for studying single track performance, or using a bremsstrahlung photon beam converted to e^+e^- pairs for studying two-track separation capability.

6.1 Experimental Apparatus

In order to test the overall performance including two-track separation capability, we constructed a test chamber with small jet cells, which is called a *baby* chamber of the proposed JLC-CDC. Fig. 23 shows a picture of the test chamber. The cross-sectional size of the test chamber is 26cm $\times$ 27cm and the wire length is 40cm. This chamber has three identical jet cells with the same cell structure as our previous 4.6m-long test chamber.

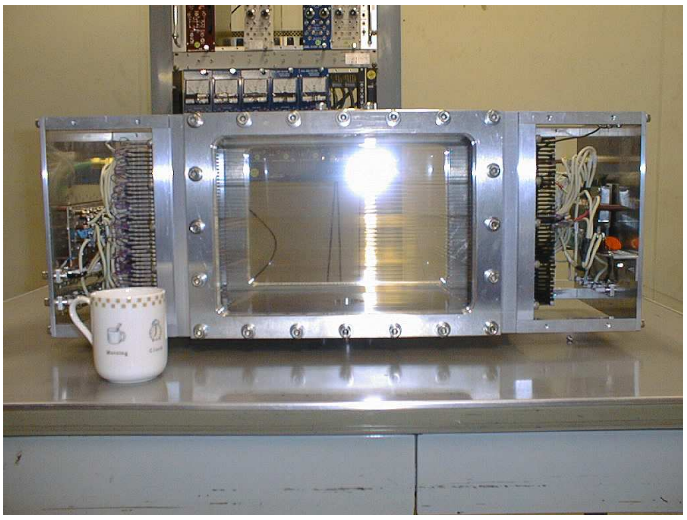

Figure 23: Baby chamber.

The experimental setup for the two-track separation study is shown in Fig. 24.

In this experiment, we used a hodoscope and a beam counter as triggering devices. The hodoscope has eight channels in both horizontal and vertical directions and each channel consists of a 2mm wide scintillation counter.

In the case of single track data taking, the electron beam extracted from the electron synchrotron (ES) was used. In the case of two-track data taking, we used a bremsstrahlung

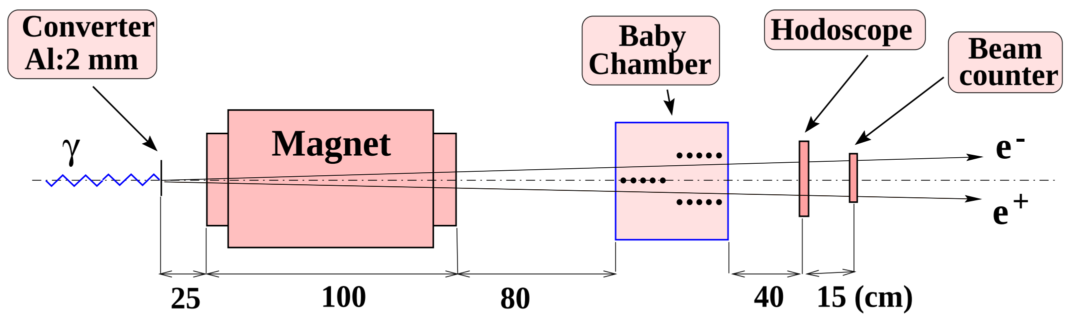

Figure 24: Setup of 2-track separation experiment.

photon beam produced at a Pt radiator. This γ-ray beam was converted to electron-positron pairs by an Al plate converter (thickness: 2 mm). These electron-positron pairs were separated vertically by a magnetic field controlled to generate two tracks with various track-to-track distance in the drift chamber.

6.2 Experimental Results

Typical signal shapes for a single and two tracks are shown in Fig. 25 as recorded by flash ADCs.

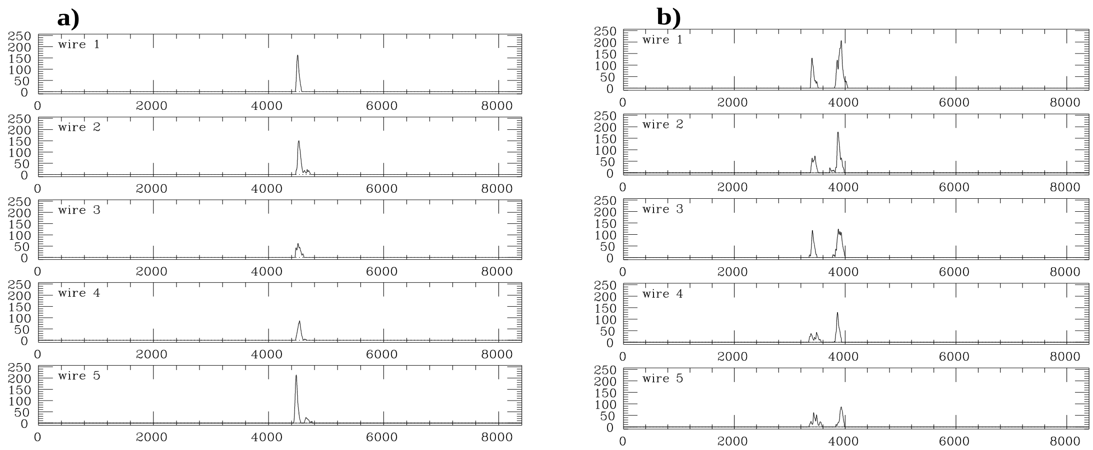

Figure 25: Typical signal shape of single (a) and two (b) tracks.

Preliminary results of spatial resolution as a function of drift length (sense wire 3) is shown in Fig. 26. As we can see the spatial resolution is less than 100 μm per wire over the full drift length. In Fig. 27 we compare the spatial resolution per wire for the *Baby* and 4.6 m-long test chambers.

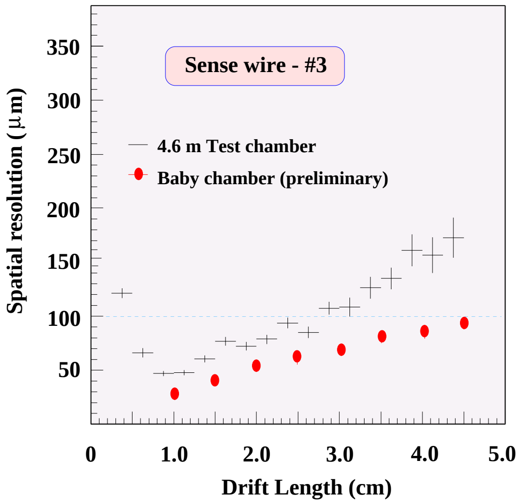

Figure 26: Spatial resolution as a function of drift distance

		S1	S2	S3	S4	S5
$\sigma_x(\mu m)$	4.6 m Chamber	117 ± 23	103 ± 7	103 ± 9	98 ± 9	109 ± 16
	Baby	75 ± 2	66 ± 2	63 ± 2	64 ± 2	74 ± 2

Figure 27: Spatial resolution per wire for *Baby* and 4.6 m long test chambers.

7 Conclusions

We have constructed a 4.6 m-long test drift chamber in the course of JLC detector R&D's. The test chamber has the same wire length, cell structure, and chamber gas (CO_2 isobutane$(90:10)$) as a current design of the JLC central drift chamber.

We have developed a wire position measurement system. Using this we measured the gravitational and electrostatic sags. The average gravitational sags for field and sense wires are 600μm and 353μm, which are in good agreement with predictions 553μm and 312μm, respectively.

We have also developed a software program to calculate wire displacements in electrostatic fields, knowing the cell structure, wire tension, and high voltage on each wire. There is a good agreement with measurements for field wires surrounding sense wires.

The performance of the 4.6 m-long test drift chamber was studied by using cosmic ray events. It is confirmed that the test chamber satisfies the required spatial resolution of 100 μm per wire in the r-ϕ plane over the full length of the chamber for an incident angle of 0 to 45° to the wires.

We have outlined a general design procedure for a long cylindrical drift chamber with small jet cells with an emphasis put on the decision process for stereo wires geometry. The procedure was illustrated, taking a concrete example of a possible central tracker for JLC. The surface field variation along an anode wire is one of the decisive factors to determine stereo geometry. We have examined the surface field variation originating from the geometrical deformation of the cell structure as a function of z (the coordinate along the chamber axis) due to stereo geometry. These field variations were estimated through explicit electric field calculations using the chamber simulation program GARFIELD. The estimated field variations were translated into gain variation along the anode wires using the gas gain data taken for this purpose and used to constrain the stereo geometry.

We have established a Lorentz angle measurement system. Using this we measured the Lorentz angle of the CO_2-isobutane gas mixture for different proportions. The results of the measurements of Lorentz angle are compared with the GARFIELD program. During the experiment we found the instability of the laser beam position at the higher magnetic fields. In order to avoid this we propose a new Lorentz angle measurement system by using two laser beams.

We have fabricated a small test chamber with the same jet cell structure as our previous 4.6m-long test chamber, in order to carry out beam tests on basic chamber performance. The small test chamber was filled with the same CO_2/Isobutane(90:10) gas mixture and was exposed to test beams at KEK-Tanashi.

We used an extracted electron beam to study single track performance and preliminary results confirmed that the test chamber satisfies the required spatial resolution of 100 μm per wire over the full drift space.

Acknowledgments

I would like to thank all the members of the JLC-CDC group for their great contribution in JLC-CDC R&D's activity.

References

[1] S. Sudou, N. Khalatyan, Y. Kurihara, T. Abe, K. Fujii, A. Sugiyama, K. Takahashi, T. Watanabe, Nucl. Instrum. Methods, A383 (1996) 391. (JLC-CDC group)

[2] Y. Kurihara, A. Yamaguchi, S. Sudo, T. Abe, K. Fujii, N. Ishihara, N. Khalatyan, T. Matsui, O. Nitoh, T. Ohama, H. Okuno, A. Sugiyama, K. Takahashi, T. Watanabe, T. Yoshida, Submitted to NIM. (JLC-CDC group)

[3] N. Khalatyan, K. Fujii, H. Okuno, T. Abe, K. Hoshina, Y. Kato, Y. Kurihara, H. Kuroiwa, T. Matsui, O. Nitoh, A. Sugiyama, K. Takahashi, T. Watanabe, T. Yoshida, NIM, A 428 (1999) 403-412 (JLC-CDC group)

[4] JLC CDC group, a paper on Lorentz angle measurement, in preparation.

[5] JLC CDC group, a paper on two-track separation paper, in preparation.

[6] JLC CDC group, a paper on Gas gain measurement, in preparation.